Experimental VLBI using NCRA 15m antenna, GMRT and ORT

Author

Drishty B. Jadia

dbjadia05@gmail.com

INDIAN INSTITUTE OF TECHNOLOGY, KANPUR

Department of Physics

Project Guide

Dr. Visweshwar Ram Marthi

viswesh@ncra.tifr.res.in

NATIONAL CENTER FOR RADIO ASTROPHYSICS, PUNE

NCRA VSRP REPORT

Visiting Students' Research Program 2024

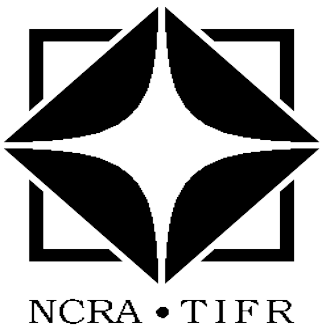

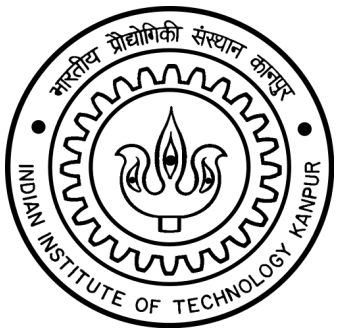

Contents

Abstract

VLBI achieves high angular resolution by combining signals from widely separated radio telescopes. In this project, we explored the feasibility of obtaining interferometric fringes on intermediate baselines using NCRA 15m antenna with GMRT at L-band (1.4 GHz), and ORT with GMRT at 325 MHz. The $\sim$ 80 km GMRT–15m baseline offers $\sim$ 0.6" resolution, while the $\sim$ 1000 km GMRT–ORT baseline provides $\sim$ 0.25". With a maximum east-west projection of $\sim$ 285 km, these baselines bridge the gap between GMRT's native resolution and intercontinental VLBI.

Since VLBI stations use independent time and frequency standards, maintaining phase stability is essential. GMRT and ORT use H-Masers, while the 15m antenna uses an OCXO. All are synchronized using GPS-disciplined Rubidium clocks. We characterized the relative stability between the OCXO and GMRT's maser, measuring a sampling clock drift of $\sim$ 17 ns/hr mainly due to OCXO frequency instability, which limits coherent integration to a few minutes.

We also measured clock offsets and applied corrections at the 15m station. While fringe detection between GMRT and the 15m failed due to timestamping issues, we successfully detected fringes between GMRT and ORT. These results confirm the potential of long-baseline VLBI using Indian facilities and identify key improvements needed for future routine operations.

Acknowledgments

I sincerely thank Dr. Vishweshwar Ram Marthi for his exceptional mentorship and continued support throughout the course of this project. His patient explanations, insightful discussions, and dedicated participation were fundamental to my understanding of VLBI and the successful execution of this work.

I am also grateful to Sandeep Chaudhari and Harshvardhan Reddy at GMRT, Khodad for their valuable assistance in setting up the experimental system and for their support in running the offline correlator. Their technical expertise and cooperation were crucial to the progress of this project.

I extend my heartfelt thanks to the National Center for Radio Astrophysics (NCRA), Pune, for providing me with the opportunity to participate in the Visiting Students' Research Program (VSRP) 2024. The program offered an enriching research environment and an excellent platform to gain hands-on experience in radio astronomy.

This work would not have been possible without the guidance and support of all the individuals and institutions mentioned above.

VLBI with Indian Radio Telescopes

1.1 Motivation and Resolution Considerations

The resolution of a telescope is limited by its aperture size. By the Rayleigh criterion, the resolution of a telescope is given by:

$$\theta \sim \frac{\lambda}{D} \tag{1.1}$$

where D is the aperture size. The spatial resolution of a telescope improves with increasing aperture diameter, enabling finer detail observation. A 300 m telescope, for eg., achieves an angular resolution of $\sim 10'$ at 1 m wavelength. However, constructing larger single-dish telescopes is impractical due to engineering and cost limitations. Interferometry addresses this by synthesizing the resolution of a telescope with an effective aperture equal to the maximum separation between smaller antennas. In this approach, resolution is determined by the longest baseline D, not the size of individual dishes.

In its basic form, radio interferometer consists of two antennas separated by distance D and connected via receivers. Linked interferometry requires physical connections, such as coaxial cables, which limit the maximum baseline. Very Long Baseline Interferometry (VLBI), however, eliminates this need, allowing telescopes to be placed thousands of kilometers apart, greatly enhancing angular resolution. Using widely separated antennas also increases the effective collecting area, improving sensitivity. Together, these features make VLBI one of the most precise and sensitive techniques for detecting radio signals from space.

In this project, we explore the feasibility of using an intermediate VLBI technique to obtain interferometric fringes across extended baselines. We use NCRA 15m antenna with Giant Metrewave Radio Telescope (GMRT) at L-band (1.4 GHz), and Ooty Radio Telescope (ORT) with GMRT at 325 MHz. The ∼80 km baseline between the NCRA 15m and GMRT provides an angular resolution of about 0.6", while the $\sim$ 1000 km baseline between GMRT and ORT achieves a resolution of $\sim$ 0.25", a significant improvement over the GMRT array's $\sim$ 2" resolution at 1.4 GHz. Signals from each baseline are independently recorded and

later combined coherently to form fringes. This demonstrates the potential of intermediate VLBI to achieve higher resolution than the GMRT array alone.

1.2 Overview of Signal Chain and Observables

The signals from the radio source arrive at the two stations at different times due to their spatial separation. The difference in the arrival times, denoted T_i, defines the observed delay between the stations, expressed as τ_{obs}. [1]

$$\tau_{obs} = T_2 - T_1 \tag{1.2}$$

To measure this delay accurately, a series of steps are followed. First, two or more radio telescopes simultaneously observe the same astronomical source. The signal received at a station, is mixed with a reference signal generated at the station (see Figure 1.1) in order to down convert it to a few hundred MHz. This down-converted signal is then digitized, time-stamped using the station's local clock, and recorded. The recorded data from all participating stations are subsequently transferred to a central correlator. At the correlator, the signals are aligned and cross-correlated. From this cross-correlation output, VLBI observables are obtained: the phase, the group delay (the derivative of the phase w.r.t. frequency) and the phase rate (the time derivative of the phase)[1].

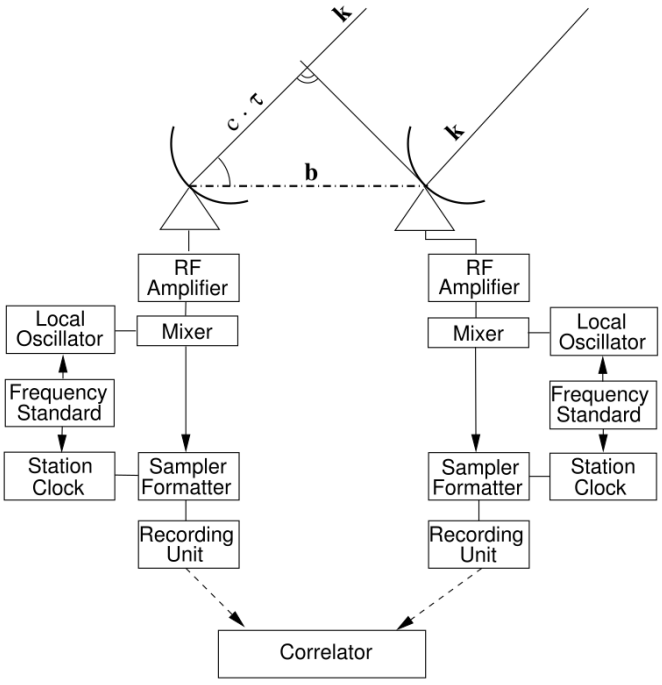

Figure 1.1: VLBI Constellation

Phase Stability of Reference Standards

2.1 Time - Frequency Standards

For the correlation process to function effectively, the recorded signals must be coherent. Any loss of coherence leads to a reduction in the signal-to-noise ratio (SNR), resulting in increased noise in the delay measurements. However, perfect coherence is difficult to maintain due to random phase fluctuations introduced by instabilities in the station reference clocks [1]. Therefore, the phase stability of the reference standard is crucial.

At GMRT, absolute time is maintained using the real-time clock (RTC) of the correlator control computer, which is synchronized with GPS-disciplined rubidium standards. The NCRA 15m antenna also relies on GPS-disciplined rubidium clocks for time referencing. The sampling clock in each of the pillars at ORT is locked to the GPS-disciplined rubidium oscillator that provides a 10-MHz reference [2]. A 1 pps signal is distributed to the pillars to ensure synchronization [3].

For Frequency standards, Atomic Hydrogen Masers (AHMs) are known for providing long-term frequency stability. GMRT and ORT uses AHMs for their frequency reference. In contrast, NCRA 15m antenna employs an oven-controlled crystal oscillator (OCXO), which, while more economical than H-masers, offers good short-term stability. To evaluate the performance of the OCXO relative to the AHM, we conducted an experiment at the GMRT Central Building to assess its phase and frequency stability.

2.2 Stability of OCXO

2.2.1 Experimental Setup

To evaluate the performance of the oven-controlled crystal oscillator (OCXO) frequency reference, we set up an experiment using two Reconfigurable Open Architecture Computing Hardware (ROACH) boards, each interfaced with an Analog-to-Digital Converter (ADC) operating at a sampling clock frequency of 300 MHz. For the purpose of this experiment, a sub-sampled rate of 75 MHz was used, and a bandwidth of 37.5 MHz was extracted and fed into the ROACH boards for processing. The ROACH boards were configured to operate with different frequency reference standards, enabling a direct comparison of their respective phase stability. The hydrogen maser (H-maser) signal was connected to the clock input of ROACH0, serving as the high-stability reference. In parallel, OCXO signal was connected to the clock input of ROACH1. This configuration enabled simultaneous digitization of the same input signal using two different frequency standards, allowing a direct analysis of the relative phase and frequency stability between the H-maser and OCXO over time.(see Figure 2.1)

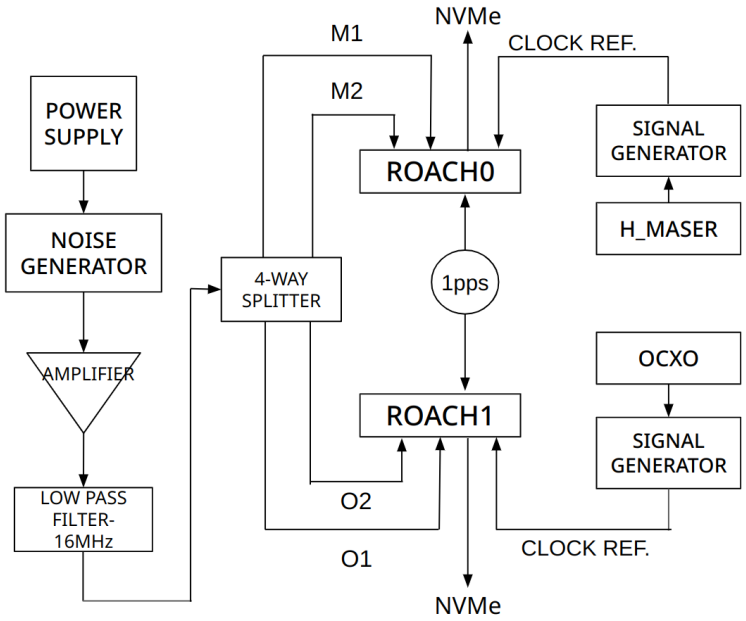

Figure 2.1: Experimental Setup

A broadband noise generator was used as the input signal source for the experiment. To ensure that the analog-to-digital converters (ADCs) received sufficient input power for optimal digitization, the noise signal was amplified using a wideband power amplifier. The amplified signal was then passed through a sequence of filters to shape the desired frequency band: first, a 100 MHz low-pass filter to remove high-frequency components, followed by a 16 MHz low-pass filter to

further narrow the bandwidth and minimize out-of-band noise.

The filtered noise signal was then fed into a 4-way power splitter, which produced four identical outputs, each with approximately one-quarter of the original signal power. These four outputs were labeled based on their association with the two frequency references: M1 and M2 for the H-maser, and O1 and O2 for the OCXO. The outputs M1 and M2 were connected to the two input channels of ROACH0, which operated with the H-maser frequency reference. Similarly, O1 and O2 were connected to the two input channels of ROACH1, referenced to the OCXO. This configuration allowed each ROACH board to process identical input signals, but under different frequency reference conditions, enabling a comparative analysis of their relative phase stability.

To ensure synchronized data acquisition across the system, a 1 pulse-per-second (1 pps) trigger—disciplined by GPS—was used to initiate simultaneous recording on both ROACH boards. The baseband voltage signals from all input channels were recorded in parallel onto high-speed dual NVMe drives for subsequent offline analysis.

2.2.2 Data Processing and Analysis

The raw data recorded were loaded into environment as a numpy array. The total duration of the recording spanned approximately two hours (7200 seconds). For each correlation analysis, two data files corresponding to a selected reference combination were processed simultaneously.

The analysis was performed in a loop, processing the data in chunks of 75 million samples per iteration, for a total of 7200 iterations—corresponding to one second of data per iteration. Each data chunk was reshaped into an array with 7500 columns to facilitate batch processing. A Fast Fourier Transform (FFT) was then applied to the reshaped data from both files at every second across the two-hour duration.

The correlation was carried out for the following combinations of input channels: M1–O1, M2–O2, M1–M2, O1–O2, and M2–O1. Prior to final analysis, initial phase offsets between the signals were corrected to ensure proper alignment. The processed cross-correlation results were then visualized through plots to examine phase stability and coherence between the signals. (see Figure 2.2) .

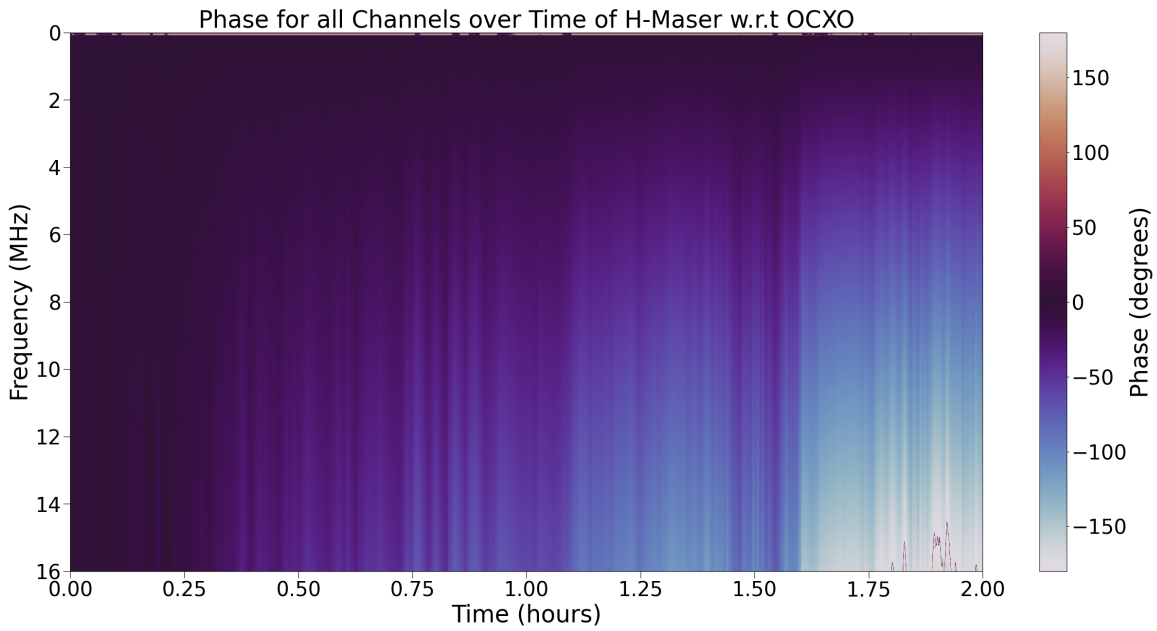

Figure 2.2: Phase Plot of M1-O1

2.2.3 Quantities Analysed

Delay Rate

The phase of the cross-power spectrum exhibits a time-dependent variation across frequency, indicating the presence of a changing delay between the two signals. This variation can be quantified by the delay rate, defined as:

$$\tau(t) = \frac{1}{2\pi}\left(\frac{d\phi}{d\nu}\right)_t \tag{2.1}$$

At each one-second interval, the phase data across the selected frequency channels—ranging from channel 750 to 1250 —was used to compute the delay. These delay values were then plotted as a function of time to generate the Delay vs Time curve. The slope of this curve (Figure 2.3) represents the delay rate, providing insight into how the relative delay between the signals evolves over the two-hour observation period.

Differential Doppler Shift

In addition to the temporal variation of phase across frequency, we also observe a frequency-dependent variation of phase over time, which corresponds to the differential Doppler shift. This is quantified by:

$$f(\nu) = \frac{1}{2\pi}\left(\frac{d\phi}{dt}\right)_\nu \tag{2.2}$$

To analyze this effect, the delay at each frequency channel was computed over the first 4500 seconds of the observation (approximately 1.5 hours). These

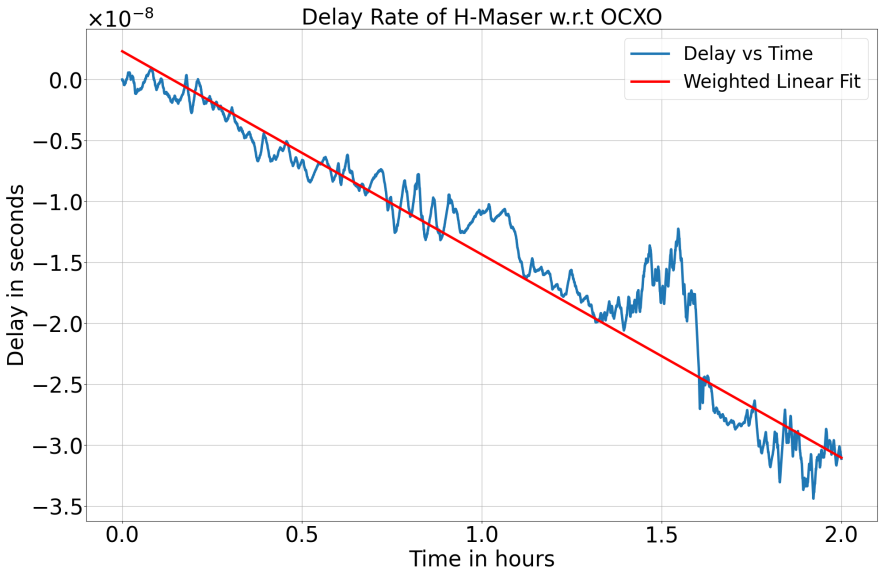

Figure 2.3: Delay Rate

delay values were then plotted as a function of frequency to generate the Delay vs Frequency curve. The slope of this plot indicates how the delay changes with frequency, revealing the presence of a differential Doppler shift between the two signals. The resulting plot, Figure 2.4 illustrates this frequency-dependent delay variation.

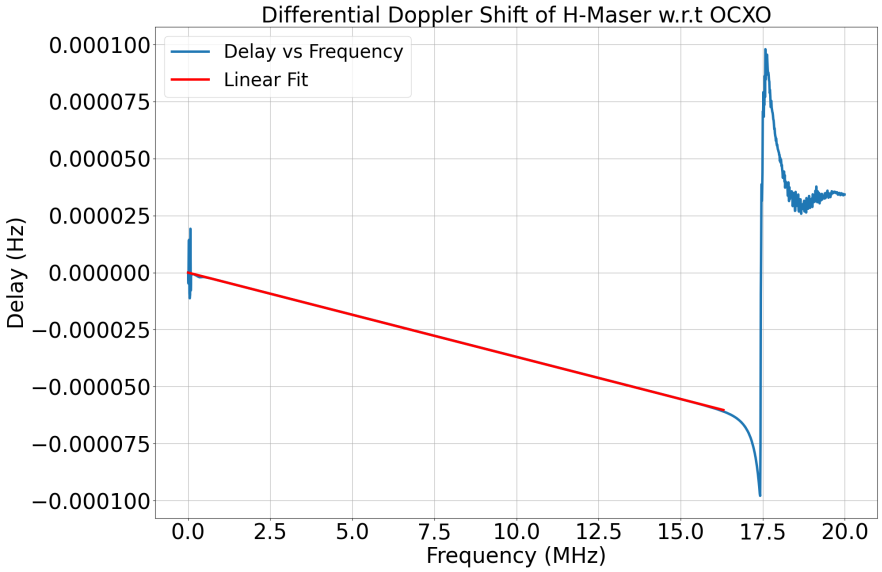

Figure 2.4: Differential Doppler Shift

Phase Closure

Phase closure is the property where the sum of the phases around a closed loop of three (or more) baselines is zero (or a constant value), modulo 2π. This property is derived from the fact that phase errors due to instrumental and atmospheric effects are largely canceled out when considering the phase differences around a closed triangle of baselines. To ensure the accuracy of our calculations, we verified the phase closure property for the combination of M1-M2-O1 at 9 MHz and 10 MHz.

2.2.4 Results

The results are based on comparing Maser w.r.t OXCO. We found the following results from our analysis:

1. Delay Rate:

   M1-O1: $-1.668 \times 10^{-08} \pm 3.544 \times 10^{-11}$ $seconds/hour$

   M2-O2: $-1.668 \times 10^{-08} \pm 3.543 \times 10^{-11}$ $seconds/hour$

2. Differential Doppler Shift:

   M1-O1: $-3.697 \times 10^{-06} \pm 5.195 \times 10^{-10}$ Hz/MHz

   M2-O2: $-3.699 \times 10^{-06} \pm 7.277 \times 10^{-10}$ Hz/MHz

We observed a drift in time of about ~ 17 ns/hr and frequency drift of about ~ 4 $\mu Hz/MHz$. For a 100 MHz bandwidth, the delay in time shall be 3 samples per hour. This highlights that OCXO is feasible for short time integrations, of the order of few minutes; because maintaining phase coherence is critical and such a drift can introduce significant phase misalignment over time.

2.3 Interpretation of Observed Trends

We observed notable trends in the phase versus time plots when looked at individual channel. We focused on the 900th, 1000th, and 1100th channels and found that the phase follows a consistent trend over time. The trend is observed before and after the initial phase correction. We suspect this trend is likely due to ADC quantization effects and floating point precision limitations. However, the variations are at the order of $1/100th$ of degree. We can safely neglect these variations.

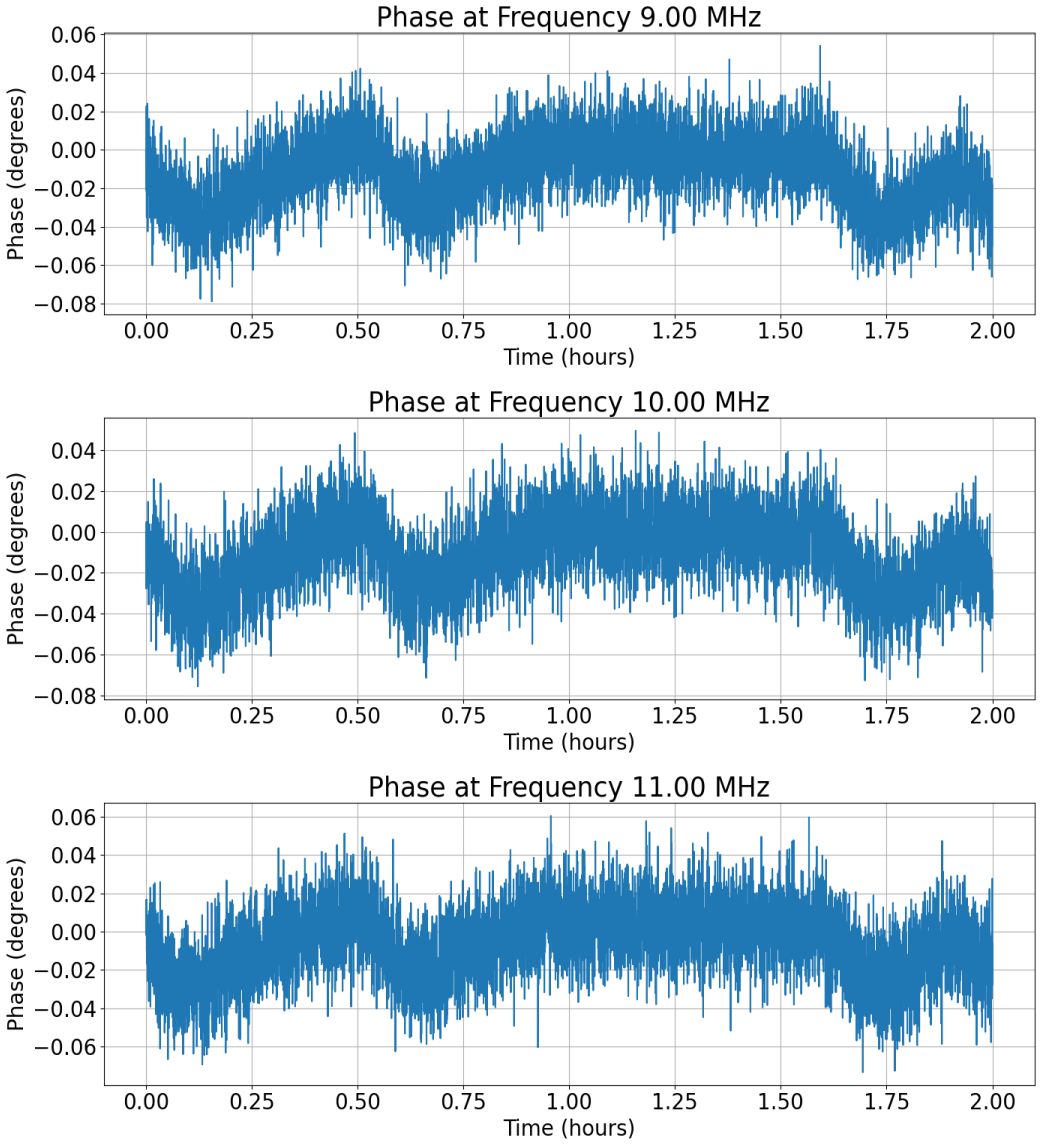

Additionally, we noticed an abrupt change in the Delay Rate plot (Figure 2.3) between $1hr\ 24min$ and $1hr\ 36min$. The cause of this anomaly is unclear, and we are uncertain about its significance and the reasons behind its occurrence.

Sensitivity of the Antenna

3.1 RMS Noise

In radio astronomy, the root mean square (RMS) noise of an antenna refers to the statistical measure of fluctuations in the received signal power due to inherent system and environmental noise. It arises primarily from thermal noise generated by the receiver electronics, the sky background (including the cosmic microwave background and galactic emission), and contributions from the atmosphere and ground spillover. RMS noise limits the sensitivity of a radio telescope, thereby constraining the minimum detectable signal. It is typically quantified using the radiometer equation, which relates RMS noise to system temperature, bandwidth, and integration time. Accurate estimation and control of RMS noise are essential for reliable detection and measurement of faint astronomical sources.

The RMS noise for the antenna:

$$\Delta I_{rms} = \frac{T_{sys}}{G\sqrt{2N(N-1)\Delta\nu\Delta\tau}} \tag{3.1}$$

where, T_{sys} is the system temperature, G is the gain of the antenna, N is the number of polarization, $\Delta\nu$ is the bandwidth used and $\Delta\tau$ is the integration time.

The RMS noise of GMRT-15m baseline is approximately 1.13 mJy with G/T_{sys} for GMRT $\approx 3.2 \times 10^{-3} Jy^{-1}$ [4] and G/T_{sys} for 15m antenna $\approx 3.4 \times 10^{-4} Jy^{-1}$ [5] for integration time of 30 minutes.

The RMS noise on a baseline between two GMRT antennas is approximately 0.37 mJy for integration time of 30 minutes.

The peak sensitivity of one full module of ORT is 150 mJy [6]

Based on the estimated sensitivity of the baselines, we determined the required time integration period for reliable detection.

Time Integration of Pulsar

4.1 The radiometer equation

For a pulsar to be detectable, its signal must exceed significantly the noise fluctuations in the receiver system. The root mean square fluctuations in T_{sys} can be expressed as:

$$\Delta T_{sys} = \frac{T_{sys}}{\sqrt{n_p t \Delta f}} \tag{4.1}$$

where Δf is the observing bandwidth, t is the integration time and $n_p = 1$ for single polarisation observations, or $n_p = 2$ if two orthogonal polarisations are summed. Equation 4.1 is called the *radiometer equation*. From this equation we derive the sensitivity of a radio source following the derivation given in [7]:

$$S_{min} = \beta \frac{(S/N)T_{sys}}{G\sqrt{n_p t_{int} \Delta f}} \sqrt{\frac{W}{P - W}} \tag{4.2}$$

where S_{mean} is the mean flux density, β is the correction factor to account system imperfections arising due to digitization of the signal, (S/N) is the signal to noise ratio, T_{sys} is the system noise temperature, G is the gain of the antenna, t_{int} is the integration time period, Δf is the observing bandwidth, W is the equivalent pulse width and P is the pulse period.

Using the equation 4.2, we estimate the necessary observation duration required for a significant pulsar detection. The key parameters - mean flux density S_{mean}, pulse width W, and pulse period P were obtained from the - ATNF Pulsar Catalogue (`https://www.atnf.csiro.au/research/pulsar/psrcat/`).

4.2 Observation Schedule and Source Selection

To ensure that observations were conducted simultaneously across the required stations, we adhered to the following schedule:

GMRT-NCRA 15m Baseline

Source	3C147
Date of Observation	28 June 2024
Time of Observation	06:00 - 06:30 UTC
Observing Band	1400 MHz
Bandwidth	100 MHz

Source	B0329+54
Date of Observation	28 June 2024
Time of Observation	06:30 - 07:00 UTC
Observing Band	1400 MHz
Bandwidth	100 MHz

GMRT-ORT Baseline

Source	3C286
Date of Observation	06 June 2024
Time of Observation	11:00 - 11:30 UTC
Observing Band	324 MHz
Bandwidth	16 MHz

Source	B0950+08
Date of Observation	06 June 2024
Time of Observation	11:30 - 12:00 UTC
Observing Band	324 MHz
Bandwidth	16 MHz

Delay Estimation Between Stations

In Very Long Baseline Interferometry (VLBI), the total delay between signals received at two stations consists of several components: the geometric delay due to the baseline vector and the source position, instrumental and propagation delays, and the clock offset arising from imperfect synchronization of station clocks. Although each station employs a GPS-disciplined 1 PPS trigger to maintain time consistency, the synchronization is not exact at the level required for coherent correlation. Factors such as the intrinsic stability of local frequency standards (e.g., OCXO, AHM), signal chain delays, and GPS disciplining errors can introduce residual clock offsets on the order of nanoseconds to microseconds. During offline correlation, only the relative time lag between signals is observed; thus, without independent knowledge of the clock behavior, the clock offset becomes degenerate with the geometric delay, both contributing indistinguishably to the measured time shift.

To estimate the delay in our VLBI setup, we observed known astronomical sources simultaneously with pairs of antennas: GMRT-NCRA 15m antenna and GMRT-ORT. The recorded signals were transferred to an offline correlator, where cross-correlation was performed to determine the relative time lag.

5.1 Between 15m and GMRT

As part of an initial test for VLBI observations, we carried out simultaneous data acquisition from the 15m antenna and the GMRT array at a central frequency of 1.4 GHz with a bandwidth of 100 MHz. The observation targeted both a standard flux calibrator, 3C147, and the bright pulsar B0329+54. Within the GMRT array, the C02 antenna was designated as the reference antenna, and its output was used for further analysis. Independent baseband recordings were made from both the 15m antenna and the GMRT C02 antenna. From the total 30-minute observation, a 30-second segment was extracted and used to perform offline cross-correlation. The correlation was computed using a custom Python-based implementation that explored a range of time lags centered around an expected delay of 1.215 seconds. The resulting cross-correlation plot showed a prominent and sharp peak within this range, indicating a strong correlation between the signals received at the two

antennas. The plot, Figure 5.1 shows the cross-correlation coefficient as a function of time lag, expressed relative to a reference delay of 1.21504 seconds in units of 50 ns. A distinct peak is observed near lag index 800, corresponding to a relative delay of approximately 1.21504 + (800 × 50 ns) seconds between the two signals. The red dashed lines mark the lag search window used to locate the correlation peak.

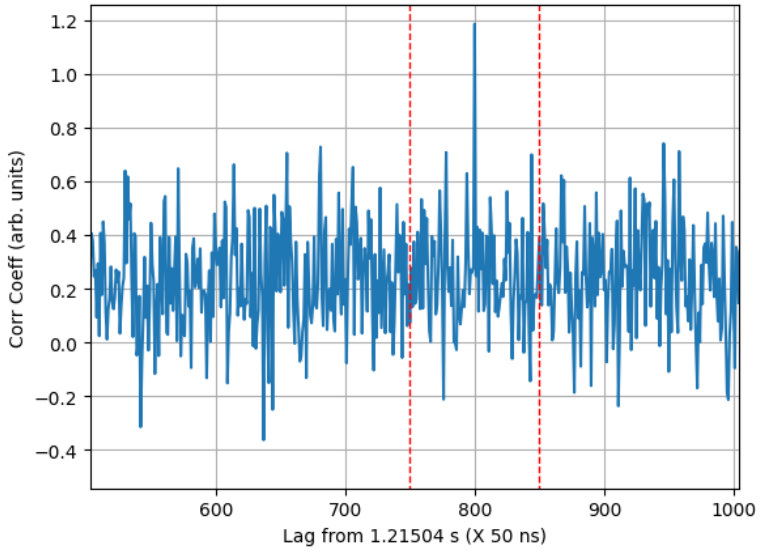

Figure 5.1: Cross-correlation between the NCRA 15m antenna and GMRT C02 antenna signals

Pulsar B0329+54 was excluded from the offset calculation because it was not detected during the observation on 28 June, despite a 15-minute integration time. This non-detection is likely due to flux variability caused by refractive interstellar scintillation, a known characteristic of this pulsar.

5.2 Between ORT and GMRT

To estimate the delay between ORT and GMRT, we observed the pulsar PSR B0950 + 08 in the 316-332 MHz frequency band. Both telescopes independently recorded raw voltage data using their respective hydrogen maser clocks and GPS-disciplined 1 PPS triggers. The primary goal was to determine the relative delay between the two stations by aligning the received pulsar signals. To do this, a pulse train was generated for each dataset, showing the periodic pulses of the observed pulsar over time. The pulse train plot helped us visually assess the relative arrival times of the pulses. By carefully comparing the alignment of these pulses, it was observed that the pulses from GMRT and ORT coincided, indicating that the delay between the stations was less than the sampling interval—thus, negligible to within one sample. This initial alignment confirmed the feasibility of further correlation, even before offline correlation was executed. The pulse train plots used in this analysis were generated by my project guide, whose support in

this stage of the project was invaluable.

The generation of the pulse train followed a standard methodology using Python. This involved converting the raw voltage data into time series format. After applying appropriate dedispersion to account for interstellar medium delays, the signal was displayed directly as a time series to retain pulse structure across stations. The aligned data streams were then plotted, with amplitude versus time showing periodic spikes characteristic of pulsar emission. The plot, Figure 5.2 shows a focused segment of the time series from three data streams: GMRT-C02 (green), South module of ORT (blue), and North module of ORT (red). A single prominent pulse from the pulsar is visible and clearly aligned across all three telescopes. The sharp coincidence of the pulse peaks indicates that the delay between the stations is within one sample, confirming sub-sample level synchronization of the recordings.

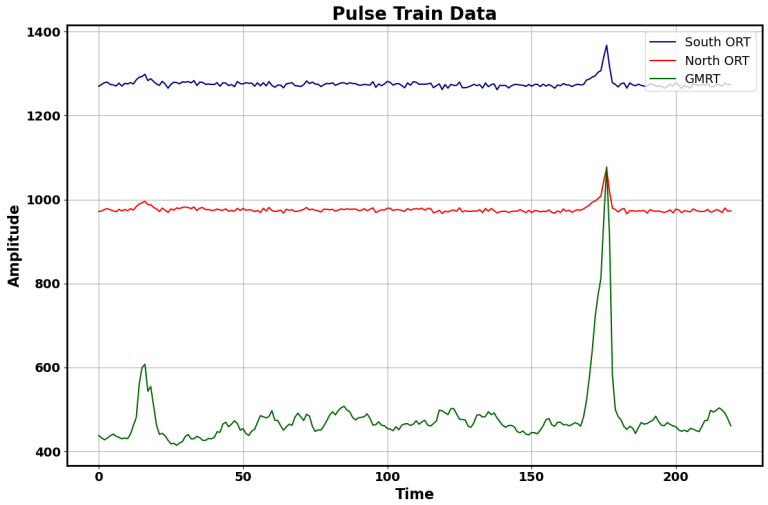

Figure 5.2: Zoomed-in view of the pulse train from PSR B0950+08 observed at GMRT and ORT.

Detection of Interferometric Fringes

6.1 For NCRA 15m Antenna and GMRT

We tried to estimate the delay between the 15-m and GMRT by searching for interferometric fringes, but we didn't see any clear fringes in the cross-correlation. We later identified that 1 PPS trigger at 15-m wasn't properly synced with its local data acquisition system. Because of that, the timestamps on the voltage samples were off, which messed up the timing alignment between the two data streams. Also, the electronic delay associated with the 15-m was not precisely characterized, further complicating delay calibration and fringe detection.

6.2 For ORT and GMRT

After visually inspecting the delay between the signals from GMRT and ORT, the offline correlation was done by a collaboration in Japan. The correlation analysis successfully yielded the detection of a fringe, Figure 6.1, confirming the presence of a coherent astronomical signal in the data recorded independently at both stations. The fringe, observed in the delay (time) domain, shows a clear correlation peak. However, the peak is not sharply localized but instead appears spread out over a wide delay range, which is atypical for ideal VLBI fringe patterns. In a perfectly calibrated system, the fringe would be concentrated around a narrow delay value corresponding to the true geometric and instrumental offset between the two stations. The broadening of the fringe suggests potential sources of residual delay or time synchronization errors that were not fully corrected during pre-processing.

One possible explanation for the broad fringe is a residual clock offset or delay smearing caused by uncompensated delay variations across the observed bandwidth. If there is any discrepancy in time tagging, or if the clocks at the two stations are not perfectly synchronized down to sub-sample precision, the resulting correlation peak can broaden, leading to reduced fringe contrast. Additionally, the signal might have experienced dispersion or instrumental delay differences that were not uniformly corrected across the band. The delay resolution of the correlator and any windowing functions applied during Fourier transformation can also affect the sharpness of the fringe. Despite these artifacts, the detection of a visible

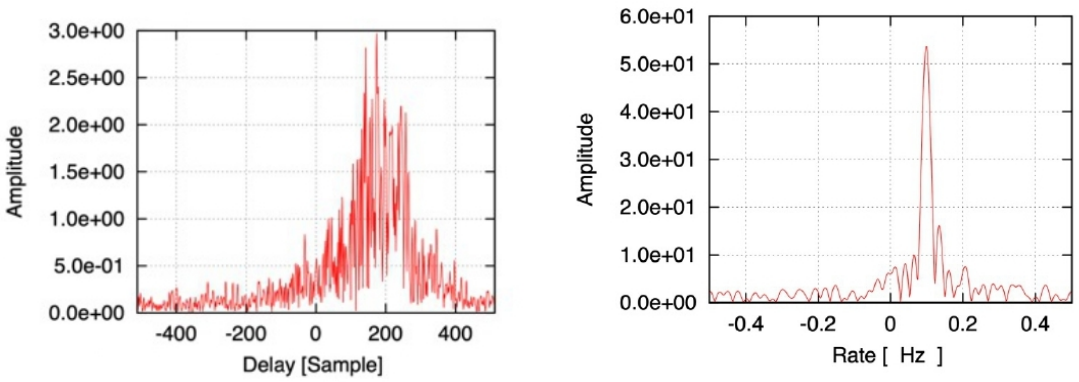

Figure 6.1: Fringe Amplitude as function of Delay and Fringe Rate

and stable correlation pattern confirms that the same sky signal was captured at both GMRT and ORT, indicating a successful VLBI observation in principle.

The cross power spectrum, Figure 6.2 further reinforces this conclusion. It shows consistent sensitivity across the entire observing band, without confinement to any narrow frequency region. This broadband coherence confirms that the correlation is not a result of random noise, radio frequency interference (RFI), or a narrowband artifact, but a true fringe arising from an astronomical source observed simultaneously at both stations. The spectral consistency across the band strongly supports the validity of the detected fringe, even though the spread in the delay domain indicates that further refinement in delay correction, clock synchronization, or correlator settings is needed to achieve higher fringe contrast. These results mark an important step toward establishing long-baseline VLBI capability between GMRT and ORT and highlight specific areas for technical improvement in future correlation attempts.

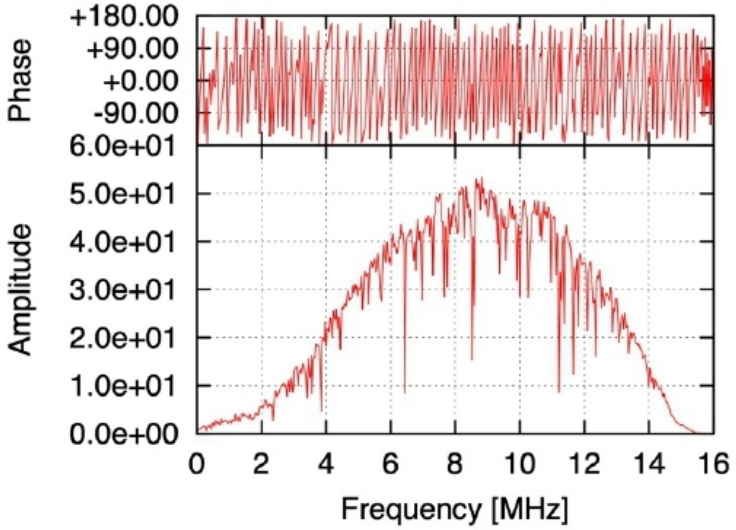

Figure 6.2: Cross-spectrum (amplitude and phase) of correlated signal

References

[1] Axel Nothnagel, Tobias Nilsson, and Harald Schuh. "Very Long Baseline Interferometry: Dependencies on Frequency Stability". In: 214.3, 66 (Apr. 2018), p. 66. DOI: 10.1007/s11214-018-0498-1.

[2] C. R. SUBRAHMANYA et al. "The Receiver System for the Ooty Wide Field Array". In: *Journal of Astrophysics and Astronomy* 38.1 (Mar. 2017). ISSN: 0973-7758. DOI: 10.1007/s12036-017-9434-0. URL: http://dx.doi.org/10.1007/s12036-017-9434-0.

[3] C. R. SUBRAHMANYA, P. K. MANOHARAN, and JAYARAM N. CHENGALUR. "The Ooty Wide Field Array". In: *Journal of Astrophysics and Astronomy* 38.1 (Mar. 2017). ISSN: 0973-7758. DOI: 10.1007/s12036-017-9430-4. URL: http://dx.doi.org/10.1007/s12036-017-9430-4.

[4] Y. Gupta et al. "The upgraded GMRT: opening new windows on the radio Universe". In: *Current Science* 113.4 (Aug. 2017), pp. 707–714. DOI: 10.18520/cs/v113/i04/707-714.

[5] Apurba Bera and Jayaram N Chengalur. "Super-giant pulses from the Crab pulsar: energy distribution and occurrence rate". In: *Monthly Notices of the Royal Astronomical Society: Letters* 490.1 (Sept. 2019), pp. L12–L16. ISSN: 1745-3933. DOI: 10.1093/mnrasl/slz140. URL: http://dx.doi.org/10.1093/mnrasl/slz140.

[6] V. R. Marthi et al. *Sensitivity measurements of dipole groups under Phases I & II of the ORT Programmable Receiver*. Test Memorandum, Radio Astronomy Centre, National Centre for Radio Astrophysics, Tata Institute of Fundamental Research, Udhagamandalam. Internal memorandum. Nov. 2011.

[7] D. R. Lorimer and M. Kramer. *Handbook of Pulsar Astronomy*. Vol. 4. 2004.